ANNUAL REVIEWS

Annual Review of Physical Chemistry

Understanding and Controlling Intersystem Crossing in Molecules

Christel M. Marian

Institute of Theoretical and Computational Chemistry, Heinrich Heine University, Düsseldorf 40204, Germany; email: Christel.Marian@hhu.de

Annu. Rev. Phys. Chem. 2021. 72:617–40

First published as a Review in Advance on February 19, 2021

The *Annual Review of Physical Chemistry* is online at physchem.annualreviews.org

https://doi.org/10.1146/annurev-physchem-061020-053433

Keywords

spin–orbit coupling, spin–spin coupling, hyperfine interaction, El-Sayed rule, energy gap law, solvent effect, heavy-atom effect, OLED emitter, aromatic ketone

Abstract

This review article focuses on the understanding of intersystem crossing (ISC) in molecules. It addresses readers who are interested in the phenomenon of intercombination transitions between states of different electron spin multiplicities but are not familiar with relativistic quantum chemistry. Among the spin-dependent interaction terms that enable a crossover between states of different electron spin multiplicities, spin–orbit coupling (SOC) is by far the most important. If SOC is small or vanishes by symmetry, ISC can proceed by electronic spin–spin coupling (SSC) or hyperfine interaction (HFI). Although this review discusses SSC- and HFI-based ISC, the emphasis is on SOC-based ISC. In addition to laying the theoretical foundations for the understanding of ISC, the review elaborates on the qualitative rules for estimating transition probabilities. Research on the mechanisms of ISC has experienced a major revival in recent years owing to its importance in organic light-emitting diodes (OLEDs). Exemplified by challenging case studies, chemical substitution and solvent environment effects are discussed with the aim of helping the reader to understand and thereby get a handle on the factors that steer the efficiency of ISC.

1. INTRODUCTION

Intersystem crossing (ISC): radiationless transition between electronic states with different spin multiplicities

Internal conversion (IC): radiationless transition between electronic states with equal spin multiplicities

For a long time, intersystem crossing (ISC) has been a topic for specialists only. The foundation for a qualitative understanding of the ISC mechanisms was laid in the 1950s through the 1970s, and these rules appeared to be sufficient guidance for the design of triplet sensitizers with applications in photodynamic therapy or as photoinitiators of radical reactions. The first new impetus came with the advent of femtosecond time-resolved spectroscopic studies showing that ISC may occur at the picosecond timescale, even in molecules composed of light elements only. Research on the mechanisms of ISC has experienced a major revival in recent years owing to its importance in optoelectronics and photonics. Before discussing the theoretical foundations of ISC, I summarize the recent developments in this fascinating field of application.

Organic light-emitting diodes (OLEDs) are energy-efficient electroluminescent devices applied in display and lightning technologies. Electrons and holes carry a spin angular momentum of 1/2. Upon their recombination in an OLED, singlet and triplet excitons are created statistically at a ratio of 1:3. To achieve an internal quantum efficiency (IQE) of 100%, singlet as well as triplet excitons have to be harvested. The first generation of OLEDs was based on fluorescent emitters that exhibit IQEs of 25% at most (1). In all following OLED generations, efficient intercombination transitions between singlet and triplet excited states are crucial (**Figure 1**). While green and red phosphorescing OLEDs have become key to today's display industry (2–6), there is a strong need for operationally stable blue light OLED emitters with IQEs close to 100% (7). To impede the degradation of transition metal complexes by dissociative ligand field states, researchers have devised compounds with large ligand field splittings such as cyclometalated carbene complexes (8–10). Recent years have witnessed rapid progress in the design of OLED materials based on thermally activated delayed fluorescence (TADF) (11–16). While the overall efficiency of the TADF process may involve several factors, there is increasing interest in the details of the donor–acceptor coupling per se (17–19). Hyperfluorescent devices aim to combine high IQE and durable operational stability by using TADF molecules as assistant dopants to conventional fluorescent emitters (20, 21). Also, phosphor-sensitized fluorescence has been discussed as a means to improve the IQEs and efficiency roll-offs of OLEDs at high luminance (22–25).

2. QUANTUM CHEMICAL DESCRIPTION

The existing framework of quantum chemistry accommodates ISC in the intermediate regime between a nonrelativistic and a fully relativistic description of matter. At the nonrelativistic level of theory, the Schrödinger equation applies, and its eigenfunctions can simultaneously be made eigenfunctions of the total electron spin $\hat{\mathcal{S}}^2$ with eigenvalues $S(S+1)$, classified according to their electron spin multiplicity $2S+1$. Because the nonrelativistic interaction Hamiltonian does not contain spin-dependent terms, transitions between states of different spin multiplicities are strictly forbidden. In relativistic quantum chemistry, S is not a good quantum number and the definition of electron spin multiplicity is not meaningful, nor does it make sense to distinguish between multiplicity-conserving [internal conversion (IC)] and -altering (ISC) processes. In the intermediate coupling regime, electron spin and spatial degrees of freedom can be separated in first order, and their interaction is treated as a perturbation.

2.1. Spin-Coupling Hamiltonians

To account for spin-magnetic interactions of the electron, Pauli (26) introduced a two-dimensional matrix representation of spin operators that would later become known as the Pauli spin matrices.

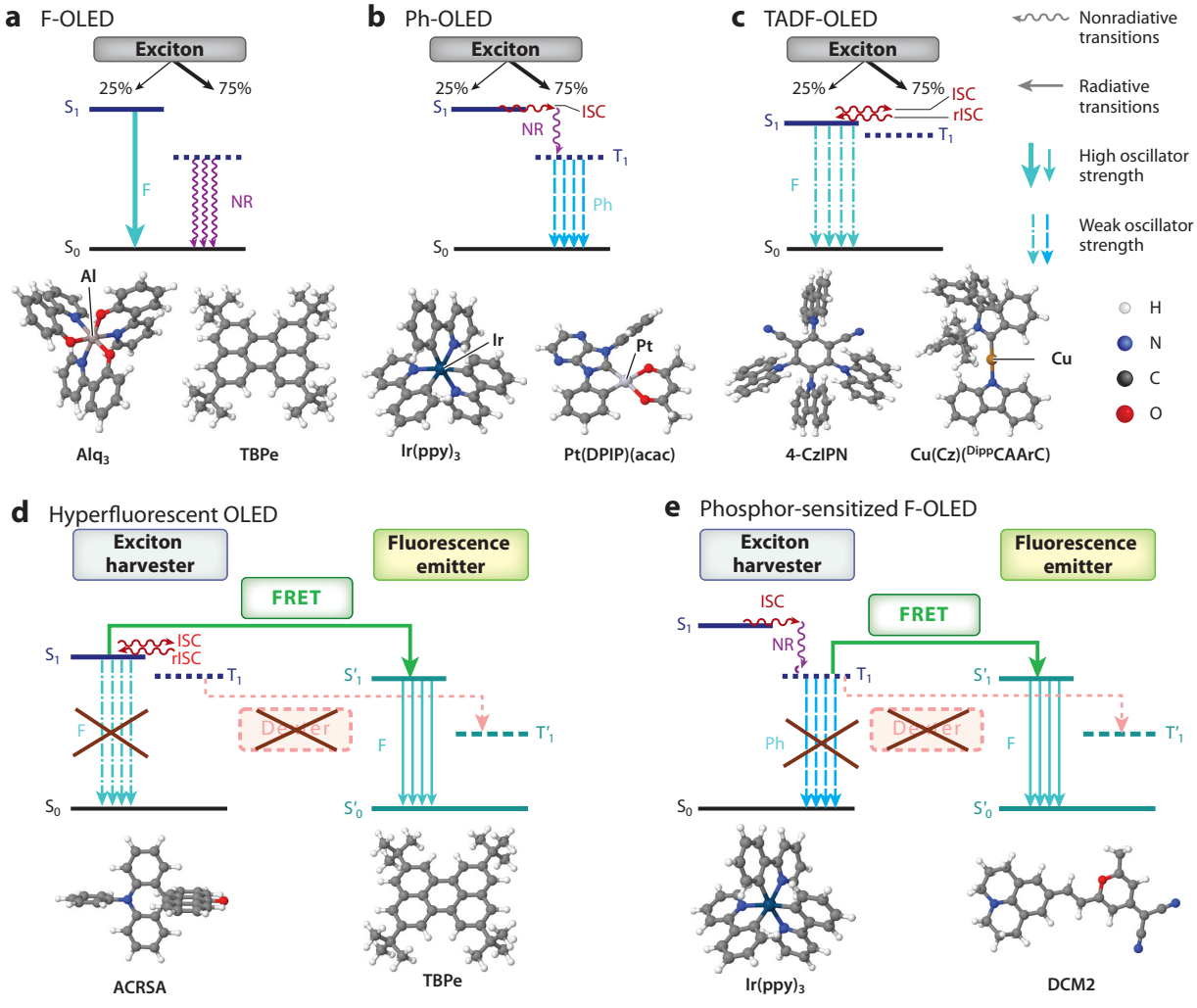

Figure 1

Exciton harvesting and luminescence mechanisms in different generations of OLED emitters. (*a*) F-OLEDs employ fluorescent emitters such as Alq_3 or polycyclic aromatic hydrocarbons, here TBPe. Triplet excitons deactivate nonradiatively. (*b*) Organometallic Ir or Pt complexes undergo fast and efficient ISC to their lowest triplet states, enabling IQEs close to 100%. (*c*) TADF-OLEDs exploit rISC to move the triplet population to the first excited singlet state, which then emits delayed fluorescence. In order for $S_1 \rightsquigarrow T_1$ rISC to be competitive with nonradiative $T_1 \rightsquigarrow S_0$ deactivation to the ground state, the S_1–T_1 energy gap ΔE_{ST} must be small in comparison to thermal energies. Typical TADF emitters are metal-free organic donor–acceptor compounds, here 4-CzIPN, or coinage metal complexes, here Cu(Cz)(^{Dipp}CAArC). (*d*) In hyperfluorescent devices, the TADF assistant dopant harvests triplet and singlet excitons and transfers its excitation energy to the strongly fluorescent acceptor by singlet FRET. Quenching of the luminescence due to Dexter energy transfer must be avoided. (*e*) Typically, Ir complexes play the role of exciton harvester in phosphor-sensitized F-OLEDs. Abbreviations: ACRSA, 10-phenyl-10H,10′H-spiro[acridine-9,9′-anthracen]-10′-one; Alq_3, 8-hydroxyquinoline aluminum(III); Cu(Cz)(^{Dipp}CAArC), {2-[2,6-bis(propan-2-yl)phenyl]-1,1-diphenyl-1H-isoindole-2-ylidene}(9H-carbazol-9-yl)copper(I); DCM2, [2-methyl-6-[2-(2,3,6,7-tetrahydro-1H,5H-benzo[i,j]-quinolizin-9-yl)ethenyl]-4H-pyran-4-ylidende]propanedinitrile; F, fluorescence; FRET, Förster resonant energy transfer; IQE, internal quantum efficiency; $Ir(ppy)_3$, *fac*-tris(2-phenylpyridine)iridium(III); ISC, intersystem crossing; NR, nonradiative transition; OLED, organic light-emitting diode; Ph, phosphorescence; Pt(DPIP)(acac), 1,3-imidazo[5,4-b]pyrazin-2-ylidene-κC^2, κ$C^{2'}$ (2,4-pentanedionato-κO,κO′)platinum(II); rISC, reverse intersystem crossing; TADF, thermally activated delayed fluorescence; TBPe, 2,5,8,11-tetra-*tert*-butylperylene; 4-CzIPN, 2,4,5,6-tetra(9H-carbazol-9-yl) isophthalonitrile.

Integrals of the matrix vector $\hat{\boldsymbol{\sigma}}$ differ from those of the spin operators $\hat{\mathbf{s}}$ by only a factor of $\hbar/2$ (27). Spin-magnetic interactions can be introduced into the nonrelativistic Hamiltonian by replacing the linear momentum operator $\hat{\mathbf{p}}$ with $\hat{\boldsymbol{\sigma}}\,\hat{\mathbf{p}}$. For a free particle, nothing is changed by this replacement. In the presence of a vector potential $e\mathbf{A}/c$, however, magnetic interaction terms result (28, 29). Spin-dependent perturbation operators can, of course, be obtained more rigorously by subjecting the four-component relativistic Dirac–Coulomb or Dirac–Breit Hamiltonians to nonrelativistic transformations (30, 31).

2.1.1. Spin–orbit coupling. Spin–orbit coupling (SOC) is by far the most important of the spin-dependent terms in the spin-coupling Hamiltonian. Because it is a Hermitian but antisymmetric operator, it does not have diagonal matrix elements unless spatially degenerate states are involved. The SOC Hamiltonian can step up or step down the total spin angular momentum S by one unit, or, to be more precise, spin–orbit coupling matrix elements (SOCMEs) vanish unless $S - S' = 0, \pm 1$ and $S + S' \geq 1$ (27).

The Breit–Pauli SOC Hamiltonian consists of one- and two-electron interaction operators and hence can couple configurations that are singly or doubly excited with respect to one another. The spin–same- and spin–other-orbit parts are often contracted into a single term that connects easily to a simplified Hamiltonian in which SOC is considered a sum of magnetic interactions between effective orbital angular momenta and electron spins:

$$\hat{\mathcal{H}}_{\mathrm{SO}}^{\mathrm{BP}} = \frac{e^2\hbar}{2m_e^2c^2}\sum_i \left\{ \sum_\nu Z_\nu \left(\frac{\hat{\mathbf{r}}_{i\nu}}{r_{i\nu}^3} \times \hat{\mathbf{p}}_i \right) - \sum_{j\neq i} \frac{\hat{\mathbf{r}}_{ij}}{r_{ij}^3} \times (\hat{\mathbf{p}}_i - 2\hat{\mathbf{p}}_j) \right\} \cdot \hat{\mathbf{s}}_i. \qquad 1.$$

In Equation 1, $\hbar$ is the Planck constant h divided by 2π, e is the charge unit, m_e is the electron mass, and c is the speed of light. The vector $\hat{\mathbf{r}}_{i\nu}$ denotes the relative position of nucleus ν with atomic number Z_ν^{eff} and electron i with linear momentum $\hat{\mathbf{p}}_i$ and spin $\hat{\mathbf{s}}_i$. In addition to the one-electron terms, the SOC operator in Equation 1 contains terms representing the mutual interactions of electrons i and j. The two-electron terms cannot be neglected, but they can be contracted into effective mean-field operators (32–34), similar to the Coulomb and exchange operators in Hartree–Fock theory. The Breit–Pauli operator in Equation 1 is well suited for computing SOC in organic molecules, but it cannot be applied in variational calculations of SOC in heavy-element compounds because it is unbounded from below. A variationally stable SOC Hamiltonian has been derived, for instance, by means of a Douglas–Kroll transformation of the Dirac–Breit Hamiltonian in no-pair approximation (35). Another can be formulated using the zero-order regular approximation to the Dirac–Coulomb equation (36). Both behave effectively like a $1/r$ potential close to a nucleus, but they are rarely employed in practical applications.

The most widespread SOC Hamiltonian is an operator that incorporates the screening of the one-electron terms due to the two-electron interactions by an effective charge (37, 38). In this approach, $\hat{\mathcal{H}}_{\mathrm{SO}}^{\mathrm{BP}}$ is approximated as

$$\hat{\mathcal{H}}_{\mathrm{SO}}^{\mathrm{eff}} = \frac{e^2\hbar^2}{2m_e^2c^2}\sum_i^n \sum_\nu^N \frac{Z_\nu^{\mathrm{eff}}}{r_{i\nu}^3}\hat{\boldsymbol{\ell}}_{i\nu}\hat{\mathbf{s}}_i, \qquad 2.$$

where $\hat{\boldsymbol{\ell}}_{i\nu} = \hat{\mathbf{r}}_{i\nu} \times \hat{\mathbf{p}}_i/\hbar$ is the orbital angular momentum and the effective charge Z_ν^{eff} is a semiempirical fit parameter. In conjunction with effective-core potentials (ECPs) for heavy elements, this fit parameter can become very large because the electron density in the pseudoorbital is very small close to the nucleus and the interaction strength between $\hat{\boldsymbol{\ell}}_{i\nu}$ and $\hat{\mathbf{s}}_i$ needs to be scaled up. In these

cases, it is preferable to employ the SOC operators derived from relativistic ECPs (39–41):

$$\hat{\mathcal{H}}_{\mathrm{SO}}^{\mathrm{ECP}}(v) = \sum_{i}^{n} \sum_{\ell=1}^{L-1} \frac{2\Delta V_\ell(r_{iv})}{2\ell+1} \hat{P}_\ell(i)\, \hat{\boldsymbol{\ell}}_{iv} \hat{\mathbf{s}}_i\, \hat{P}_\ell(i). \qquad 3.$$

Here, $\Delta V_\ell(r_{iv})$ denotes the difference of the fully relativistic ECPs for the $j = \ell + 1/2$ and $j = \ell - 1/2$ atomic spinors and L is the maximum orbital angular momentum quantum number employed in the local part of the ECP. The projection operators $\hat{P}_\ell(i)$ ensure that the correct spin–orbit potential is applied to electrons in orbitals with angular momentum ℓ (42). The use of these projectors enables the definition of different effective SOC potentials for p, d, and f shells in one spin–orbit ECP. A spin–orbit ECP on a heavy element can be mixed with other one-center SOC Hamiltonians, such as atomic mean-field integral approximations on lighter elements (43).

2.1.2. Spin–spin coupling. If first-order SOC is small or vanishes by symmetry, ISC can proceed by alternative mechanisms such as electronic spin–spin coupling (SSC). In Breit–Pauli theory, the magnetic dipole interaction of two electronic spins is described by the following microscopic Hamiltonian:

$$\hat{\mathcal{H}}_{\mathrm{SS}}^{\mathrm{BP}} = \frac{e^2\hbar^2}{m_e^2 c^2} \sum_i \sum_{j\neq i} \left\{ -\frac{8\pi}{3}\delta(\hat{\mathbf{r}}_{ij})\hat{\mathbf{s}}_i\hat{\mathbf{s}}_j + \frac{\hat{\mathbf{s}}_i\hat{\mathbf{s}}_j}{r_{ij}^3} - 3\frac{(\hat{\mathbf{r}}_{ij}\hat{\mathbf{s}}_i)(\hat{\mathbf{r}}_{ij}\hat{\mathbf{s}}_j)}{r_{ij}^5} \right\}. \qquad 4.$$

The term containing the δ function describes the spin-magnetic interaction of two electrons located at the same point in space and does not have a classical analog. The second and third terms are the quantum mechanical equivalents of the classical dipolar interaction term. Together, these terms form a compound tensor operator of rank zero (i.e., a scalar) consisting of a second-rank tensor with five independent spatial components (i.e., a traceless, symmetric three-by-three matrix) and the two first-rank spin operators, $\hat{\mathbf{s}}_i$ and $\hat{\mathbf{s}}_j$. Accordingly, SSC vanishes between pairs of states unless $S - S' = 0, \pm 2$ and $S + S' \geq 2$.

Unlike SOC, SSC can mix singlet and quintet states in first order. It has therefore been argued that SSC is responsible for the deviations from the putative spin statistical limit of 1/9 singlet quantum yield upon recombination of ^{1,3,5}(T...T) triplet pair states in several triplet–triplet upconversion annihilation systems (44, 45). Furthermore, there are indications that fine-structure interactions participate in the reverse process, singlet fission, as well (46–48). In the limiting case where the spin-magnetic interactions of the triplet pair states are larger than or comparable to their electrostatic splittings, the ^{1}(T...T) and ^{5}(T...T) states are expected to be mixed by electronic SSC. Also, second-order SOC to intermediate triplet states might contribute to this multiplet coupling.

2.1.3. Hyperfine coupling. Magnetic dipole–dipole interactions of the nuclear spin $\hat{\boldsymbol{\mathcal{I}}}$ and the electron spin $\hat{\mathbf{s}}$ can couple states of different electron spin multiplicities as well. They are combined into the hyperfine interaction (HFI) Hamiltonian

$$\hat{\mathcal{H}}_{\mathrm{HFI}} = \frac{e^2\hbar^2 g_e}{4m_e m_p c^2} \sum_v \sum_i g_{N_v} \left\{ \frac{8\pi}{3}\hat{\boldsymbol{\mathcal{I}}}_v\hat{\mathbf{s}}_i\delta(r_{iv}) + \frac{\hat{\boldsymbol{\mathcal{I}}}_v\hat{\boldsymbol{\ell}}_{iv}}{r_{iv}^3} - \frac{\hat{\boldsymbol{\mathcal{I}}}_v\hat{\mathbf{s}}_i}{r_{iv}^3} + 3\frac{(\mathbf{r}_{iv}\hat{\boldsymbol{\mathcal{I}}}_v)(\mathbf{r}_{iv}\hat{\mathbf{s}}_i)}{r_{iv}^5} \right\}, \qquad 5.$$

where m_p is the proton mass and g_e and g_{N_v} are the electronic and nuclear g factors, respectively. The first term in Equation 5 represents the isotropic Fermi contact interaction. Because of the

δ function, this interaction is operative only very close to the nucleus and vanishes for all but *s* electrons. The second term is a nuclear spin–electronic orbit coupling term. The expressions describing the dipolar interactions of the nuclear and electronic spin-magnetic moments (third and fourth terms in Equation 5) are completely analogous to the electronic SSC terms in Equation 4. However, the proton mass m_p is approximately 1,836 times larger than the electron mass m_e, while the electronic and nuclear *g* factors are in the same ballpark: g_e has a value close to 2.0023, whereas g_{N_v} is specific for every nucleus. For a proton, it has a value close to 5.5857. Therefore, the constant prefactor, scaling the interactions in Equation 5, is three orders of magnitude smaller than the corresponding prefactor in Equation 4. The effect of the much smaller nuclear magnetic dipole moments can be partially compensated for by closer spatial proximity. Some authors postulate that ISC and reverse ISC (rISC) between charge-transfer (CT) states of donor–acceptor complexes are driven by dipolar proton–electron HFIs (49), whereas others suggest that spin–vibronic interaction of the CT states and close-by locally excited (LE) states mediate ISC and rISC in such compounds (18, 50–52).

2.2. Transition Probabilities

The solution of the time-independent Schrödinger equation yields stationary states, that is, states that live forever. To obtain an expression for the probability of transition between two states, one must take into consideration the time evolution of the state populations. Two major routes can be followed to achieve this goal: (*a*) dynamic approaches that explicitly propagate the solutions of the time-dependent Schrödinger equation in time and (*b*) static approaches that rest on a perturbational treatment of the time dependency and determine transition probabilities in the statistical limit.

In conjunction with ISC, mostly static approaches have been employed owing to the long timescales of spin-forbidden transitions that can be handled well by perturbation theory but are cumbersome for nuclear dynamics simulations. Recently, more and more nonadiabatic dynamics simulations of ISC transitions have been performed (53–59). It is not only the higher availability of computational power that has led to this evolution. The kinetics scheme of nonadiabatic transitions involving more than two electronic states simultaneously is very difficult to handle within a static approach. As I am not an expert in the field of excited-state dynamics of spin-forbidden transitions, I refer the reader to recent review articles for details on that topic (18, 52). In the following subsections, emphasis is placed on the static picture.

2.2.1. The Fermi golden rule. Time-dependent perturbation theory employing a time-independent perturbation yields an equation that is commonly known as the Fermi golden rule expression for the transition probability of a radiationless transition. Within the framework of the Born–Oppenheimer approximation, nuclear and electronic degrees of freedom are approximately decoupled. In a basis of pure-spin Born–Oppenheimer states, the Fermi golden rule expression for SOC-mediated ISC from an initial vibronic state with electronic singlet wave function Ψ_{S_a} and vibrational wave function v_{aj} to a triplet state $\Psi_{T_b^\alpha}$ with fine-structure levels α and a set of vibrational states $\{v_{bk}\}$ reads as follows:

$$k_{\mathrm{ISC}_{ab}} = \frac{2\pi}{\hbar} \left| \sum_k \sum_\alpha \left\langle v_{bk}, \Psi_{T_b^\alpha} | \hat{\mathcal{H}}_{\mathrm{SO}} | \Psi_{S_a}, v_{aj} \right\rangle \right|^2 \delta(E_{aj} - E_{bk}). \qquad 6.$$

Here, the $\delta(E_{aj} - E_{bk})$ term ensures energy conservation. The perturbation theory approach is valid under the preconditions that the mutual interaction of the electronic states is small compared

CONDON APPROXIMATION

In the Condon approximation, the transition probability of an energy-conserving nonradiative transition depends quadratically on a constant electronic coupling matrix element and the overlaps of the vibrational wave functions. If the initial state is spatially degenerate or a higher-multiplicity state, the rate constants are determined separately for every component and then averaged.

with their adiabatic energy difference and that the density of final states at the energy of the initial state is high. Conversely, the Fermi golden rule approximation cannot be applied to ultrafast nonadiabatic transitions via conical intersection funnels or to systems where interference effects and recurrences are to be expected. In the latter cases, nonadiabatic nuclear dynamics simulations are mandatory for solving the kinetic equations.

2.2.2. The Condon approximation. The Condon approximation rests on the assumption that the electronic coupling strength does not change markedly upon nuclear distortion. Typically, the minimum geometry of the initial state $\{Q\}_0$ is chosen as the reference point. The rate in Equation 6 can then be simplified to

$$k_{\mathrm{ISC}_{ab}}^{\mathrm{FC}} = \frac{2\pi}{\hbar} \sum_{\alpha} \left| \langle \Psi_{\mathrm{T}_b^\alpha} | \hat{\mathcal{H}}_{\mathrm{SO}} | \Psi_{\mathrm{S}_a} \rangle \right|_{\{Q\}_0}^2 \sum_k |\langle v_{bk} | v_{aj} \rangle|^2 \, \delta(E_{aj} - E_{bk}) \qquad 7.$$

$$= \frac{2\pi}{\hbar} \sum_{\alpha} \left| \langle \Psi_{\mathrm{T}_b^\alpha} | \hat{\mathcal{H}}_{\mathrm{SO}} | \Psi_{S_a} \rangle \right|_{\{Q\}_0}^2 \mathrm{FCWD}, \qquad 8.$$

where FCWD stands for Franck–Condon weighted density of final states at the energy of the initial state (see the sidebar titled Condon Approximation).

2.2.3. Temperature. The possibility of including temperature effects in the rate equations is crucial for modeling uphill processes, such as rISC from a lower-lying T_1 state to the S_1 state. Instead of employing a single initial vibronic state, a Boltzmann distribution of vibrational state populations in the initial electronic state is assumed. At a temperature T, the rate constant for rISC from a triplet state with fine-structure components $\Psi_{\mathrm{T}_b^\alpha}$ and Boltzmann-populated vibrational wave functions $\{v_{bk}\}$ to a set of vibronic states with singlet wave function Ψ_{S_a} and vibrational wave functions $\{v_{aj}\}$ is given in the Condon approximation by (60)

$$k_{\mathrm{rISC}_{\mathrm{ba}}}^{\mathrm{FC,T}} = \frac{2\pi}{3\hbar Z} \sum_{\alpha} \left| \langle \Psi_{\mathrm{S}_a} | \hat{\mathcal{H}}_{\mathrm{SO}} | \Psi_{\mathrm{T}_b^\alpha} \rangle \right|_{\{Q\}_0}^2 \sum_k e^{\frac{-(E_{bk} - E_{b0})}{k_{\mathrm{B}} T}} \sum_j |\langle v_{aj} | v_{bk} \rangle|^2 \, \delta(E_{bk} - E_{aj}), \qquad 9.$$

where k_{B} is the Boltzmann constant and $Z = \sum_k e^{[-(E_{bk} - E_{b0})]/k_{\mathrm{B}} T}$ is the partition function of the initial triplet state. The factor 3 in the denominator on the right-hand side accounts for the averaging over the nearly degenerate triplet components.

2.2.4. Beyond the Condon approximation. If direct (i.e., first-order) SOC of two electronic states is relatively small, the assumptions underlying the Condon approximation have to be questioned. There are numerous examples where nuclear motion was proven to have a large impact on

the ISC probability and where the strict separation of electronic and vibrational degrees of freedom had to be abandoned in order to obtain meaningful computational results (18). Essentially two approaches to include the coupling of vibrational and electronic degrees of freedom have been pursued. Although the theories behind the two approaches fundamentally differ, in practice the results are very similar.

In Herzberg–Teller (HT)-type schemes of vibronic SOC, formally only the initial and final electronic states and the corresponding vibrational levels are involved. The first-order SOCME is expanded into a Taylor series in a set of mass-weighted normal coordinates {**Q**} about a reference point Q_0. Using the same nomenclature as in Section 2.2.2 and terminating the expansion after the linear term, one obtains (61)

$$k_{\mathrm{ISC_{ab}}}^{\mathrm{FC+HT}} = \frac{2\pi}{\hbar} \left| \sum_k \sum_\alpha \langle v_{bk} \mid \langle \Psi_{\mathrm{T}_b^\alpha} \mid \hat{\mathcal{H}}_{\mathrm{SO}} | \Psi_{\mathrm{S}_a} \rangle \right|_{\{Q\}_0} + \sum_A \left. \frac{\partial \langle \Psi_{\mathrm{T}_b^\alpha} \mid \hat{\mathcal{H}}_{\mathrm{SO}} | \Psi_{\mathrm{S}_a} \rangle}{\partial \mathbf{Q}_A} \right|_{\{Q\}_0} \mathbf{Q}_A \mid v_{aj} \rangle \Bigg|^2 \delta(E_{aj} - E_{bk}), \quad 10.$$

where A labels the normal modes of the initial state. Squaring yields a pure Franck–Condon (FC) term, a mixed FC/HT term, and an HT/HT term. HT-type expressions for vibronic ISC rate constants including temperature effects have been implemented by several groups (62–64). The derivatives of the SOCMEs in Equation 10 implicitly contain contributions from configuration interaction with third-party states, making a strict distinction between vibrational spin–orbit and spin–vibronic couplings difficult.

In addition to second-order SOC, two spin–vibronic coupling Hamiltonians are obtained which involve nonadiabatic coupling to intermediate states by the nuclear kinetic energy operator $\hat{\mathcal{T}}_N$; the first one invokes nonadiabatic coupling in the singlet and the second in the triplet manifold (65). For an $\mathrm{S}_a \sim \mathrm{T}_b$ transition, these read as follows:

$$\hat{\mathcal{H}}_{\mathrm{SO}}^{(2)} = \sum_c \frac{\hat{\mathcal{H}}_{\mathrm{SO}} | \Psi_{\mathrm{T}_c} \rangle \langle \Psi_{\mathrm{T}_c} \mid \hat{\mathcal{H}}_{\mathrm{SO}}}{E_{\mathrm{T}_c} - E_{\mathrm{S}_a}}, \quad 11.$$

$$\hat{\mathcal{H}}_{\mathrm{SO}}^{\mathrm{NAC}} = \sum_d \frac{\hat{\mathcal{H}}_{\mathrm{SO}} \mid \Psi_{\mathrm{S}_d} \rangle \langle \Psi_{\mathrm{S}_d} \mid \hat{\mathcal{T}}_N}{E_{\mathrm{S}_d} - E_{\mathrm{S}_a}} + \sum_e \frac{\hat{\mathcal{T}}_N | \Psi_{\mathrm{T}_e} \rangle \langle \Psi_{\mathrm{T}_e} \mid \hat{\mathcal{H}}_{\mathrm{SO}}}{E_{\mathrm{T}_e} - E_{\mathrm{S}_a}}. \quad 12.$$

An example of the enhancement of ISC and rISC by nonadiabatic interactions is ACRXTN, a donor–acceptor assistant dopant composed of a dimethylacridine donor moiety and a xanthone acceptor moiety arranged perpendicularly (**Figure 2**). In addition to closely spaced ^{1}CT and ^{3}CT states, low-lying ^{1}LE and ^{3}LE xanthone states are found (66). In the ground-state geometry [reaction coordinate (RC) = 0], the states are qualitatively well described by one configuration each. The $^3\mathrm{CT}(\pi'\pi^*)$ and $^1\mathrm{CT}(\pi'\pi^*)$ spatial configurations are nearly identical; therefore, the mutual SOC of the CT states is close to zero. Similar arguments hold for the $^3\mathrm{LE}(n\pi^*)$ and $^1\mathrm{LE}(n\pi^*)$ pair of states. The only appreciably sized singlet–triplet interaction among the low-lying states connects the $^3\mathrm{LE}(\pi\pi^*)$ and $^1\mathrm{LE}(n\pi^*)$ configurations, which differ by a single excitation. Both the n and π orbitals, involved in the excitation, exhibit nonvanishing electron density distributions on the carbonyl oxygen. The course of the SOCMEs along the reaction coordinate, displayed in **Figure 2*c***, also reveals that the Condon approximation is no longer valid for RC > 0.6. Upon C=O bond stretch, configuration interaction leads to an admixture of CT and $(n\pi^*)$ character

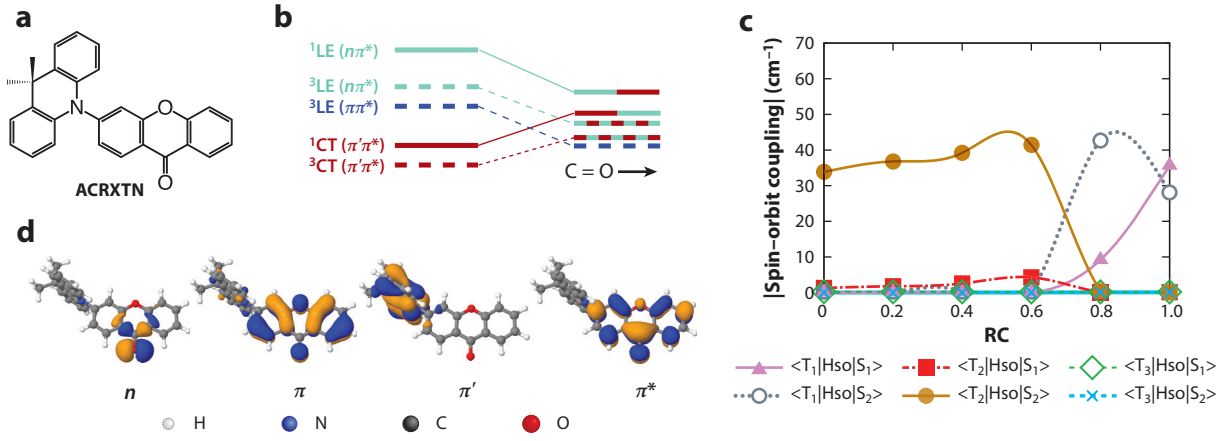

Figure 2

Vibronically mediated ISC and rISC in the TADF assistant dopant ACRXTN. (*a*) Chemical structure of ACRXTN. (*b*) Energy level scheme illustrating the course of the low-lying CT and LE states upon the C=O bond stretch. The admixture of LE($n\pi^*$) character into the T_1 and S_1 wave functions causes their mutual SOCME to rise (see panel *c*), thus enhancing the ISC and rISC probabilities markedly. (*c*) SOCMEs of the adiabatic states along an interpolated path connecting the ^{1}CT (RC = 0) and the ^{1}LE($n\pi^*$) minima (RC = 1). (*d*) Molecular orbitals involved in the ISC and rISC transitions. Abbreviations: ACRXTN, 3-[9,9-dimethylacridin-10(9H)-yl]-9H-xanthen-9-one; CT, charge transfer; ISC, intersystem crossing; LE, locally excited; RC, reaction coordinate; rISC, reverse intersystem crossing; SOCME, spin–orbit coupling matrix element; TADF, thermally activated delayed fluorescence.

in the adiabatic wave functions. The dominant mechanism of ISC and rISC in this TADF assistant dopant, therefore, is spin–vibronic coupling involving two CT states and three LE electronic states (18, 66).

3. QUALITATIVE RULES

Before it became computationally feasible to evaluate the kinetics of molecular excited-state processes by means of quantum chemistry, model theories were established to explain experimentally observed trends for ISC rate constants and triplet quantum yields. Although the predictions of these relatively closed mathematical theories occasionally fail due to the complexity of the physical phenomena and the assumptions and approximations made in their derivation, the analytical expressions provide valuable qualitative rules for estimating rate constants of ISC processes even today.

3.1. Electronic Couplings: The Generalized El-Sayed Rule

In his historical papers on the probability of spin-forbidden transitions between states of different multiplicity in nitrogen heterocyclics, El-Sayed (67, 68) formulated the rule that, to first order, there is no SOC between singlet and triplet states of the same configuration; that is, $\langle^1(n\pi^*)|\hat{\mathcal{H}}_{SO}|^3(n\pi^*)\rangle = 0$ and $\langle^1(\pi\pi^*)|\hat{\mathcal{H}}_{SO}|^3(\pi\pi^*)\rangle = 0$. For the coupling between states of different configurations, he concluded that, for instance, $|\langle^1(n\pi^*)|\hat{\mathcal{H}}_{SO}|^3(\pi\pi^*)\rangle|^2$ is much larger than $|\langle^1(\pi\pi^{*\prime})|\hat{\mathcal{H}}_{SO}|^3(\pi\pi^*)\rangle|^2$ and, therefore, that $^1(n\pi^*) \rightsquigarrow ^3(\pi\pi^*)$ ISC is much more efficient than $^1(\pi\pi^{*\prime}) \rightsquigarrow ^3(\pi\pi^*)$. Today, the International Union of Pure and Applied Chemistry (IUPAC) (69) has agreed on a more general formulation of the El-Sayed rule, which I extend by four conditions (see the sidebar titled Generalized El-Sayed Rule).

GENERALIZED EL-SAYED RULE

The rate of ISC is relatively high if the radiationless transition involves a change of orbital type, provided that:

1. The leading configurations are singly excited with regard to one another.
2. The excitation is local in nature; that is, the two singly excited orbitals exhibit nonnegligible electron density distributions on the same centers.
3. The local orbital angular momentum ℓ is conserved, and its magnetic quantum number m_ℓ changes by 1 at most:
   $\Delta\ell = 0$ and $\Delta m_\ell = \begin{cases} 0 \text{ unless } m_\ell = 0 \\ \pm 1 \end{cases}$.
4. The spin multiplicities differ by ± 2.

To understand this rule and the conditions under which it applies, let us consider only the orbitals involved in the transition and an SOC Hamiltonian in its simplest form, that is, a sum of effective one-electron operators (Equation 2). This operator couples configurations that differ by exactly one orbital occupation, namely single excitations. Integrals of genuine two-electron SOC operators that cannot be contracted to effective one-electron terms involve only valence-shell orbitals (27). Therefore, doubly excited configurations possess small mutual SOCMEs. The locality condition is derived from the r_{jv}^{-3} dependence of the one-electron interaction. Ideally, the two atomic orbitals are located at the same center to generate large SOC integrals. Conversely, SOC between CT and LE states is small.

From the fact that the angular momentum operator $\hat{\boldsymbol{\ell}} = \hat{\mathbf{r}} \times i\boldsymbol{\nabla}$ is a purely imaginary operator and is therefore antisymmetric upon Hermitian adjugation, it immediately follows that $\hat{\boldsymbol{\ell}}$ does not have diagonal matrix elements in a basis of real wave functions. Within a set of Cartesian p orbitals, nonzero matrix elements are obtained for $\langle p_x|\hat{\ell}_z|p_y\rangle$, $\langle p_x|\hat{\ell}_y|p_z\rangle$, and $\langle p_y|\hat{\ell}_x\,|\,p_z\rangle$; in other words, $\hat{\boldsymbol{\ell}}$ couples only pairs of p orbitals that are perpendicular to each other. In aromatic organic molecules, therefore, out-of-plane p orbitals forming the π system are coupled only to in-plane p orbitals, from which the nonbonding n lone-pair orbitals and the bonding and antibonding σ and σ^* orbitals are built. While $p_0 = p_z$ is an eigenfunction of the $\hat{\ell}_z$ operator with eigenvalue $m_\ell = 0$, linear combinations of p_x and p_y form the spherical p functions with eigenvalues $m_\ell = \pm 1$; that is, $p_{\pm 1} = \mp(p_x \pm ip_y)/\sqrt{2}$. Together, these relations translate into the Δm_ℓ selection rule for matrix elements of the angular momentum operators applied to p orbitals (**Figure 3*a***). Similar considerations hold for matrix elements of d orbitals (**Figure 3*b***), which are the major source of SOC in transition metal compounds. Here, $d_0 = d_{z^2}$ is the eigenfunction of $\hat{\ell}_z$ with eigenvalue $m_\ell = 0$, $d_{\pm 1} = \mp(d_{xz} \pm id_{yz})/\sqrt{2}$, and $d_{\pm 2} = \pm(d_{x^2-y^2} \pm id_{xy})/\sqrt{2}$. Due to the tensor properties of $\hat{\boldsymbol{\ell}}$ (27), $\Delta m_\ell = \pm 2$ is excluded. Note, however, that electronic states of organometallic complexes typically have multiconfigurational characters. The rules can nevertheless be applied to estimate the interaction strengths of the leading wave-function components.

The p_y (n) and p_x (π) holes associated with ($n\pi^*$) and ($\pi\pi^*$) excitations, respectively, are efficiently coupled by the z components of the $\hat{\boldsymbol{\ell}}_i$ operators. To understand why the corresponding $\hat{s}_{zi}$ operators can couple singlet and triplet spin functions, we need to construct properly antisymmetrized two-electron wave functions. The spin part of a two-electron singlet wave function is given by $[\alpha(1)\beta(2) - \beta(1)\alpha(2)]/\sqrt{2}$. Application of $\hat{s}_{z1}$ to the first term, $\alpha(1)\beta(2)$, does not change much, save for multiplication by a constant factor of 1/2. When acting on the second term, $-\beta(1)\alpha(2)$, $\hat{s}_{z1}$ also flips its sign. In total, $[\alpha(1)\beta(2) + \beta(1)\alpha(2)]/2\sqrt{2}$ is obtained, that is, up to a

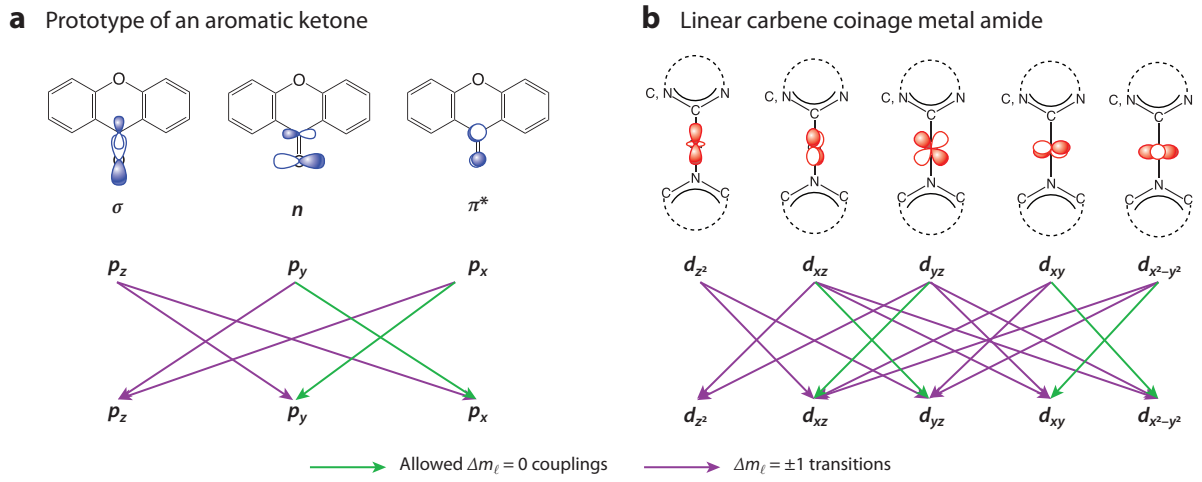

Figure 3

Illustration of the Δm_ℓ selection rule. Green arrows represent allowed $\Delta m_\ell = 0$ couplings; purple arrows, $\Delta m_\ell = \pm 1$ linkages. $\Delta m_\ell = \pm 2$ transitions are forbidden. (*a*) Cartesian *p* orbitals in a typical aromatic ketone with El-Sayed-allowed orbital couplings. (*b*) Cartesian *d* orbitals in a linear coinage metal carbene complex with El-Sayed-allowed orbital couplings.

factor of 1/2 of the triplet spin function with $m_\ell = 0$. Similar considerations apply to $\hat{s}_{z2}$. In summary, coupling of the singlet and triplet two-electron wave functions is achieved by the combined actions of $\hat{\ell}_{z1}\hat{s}_{z1} + \hat{\ell}_{z2}\hat{s}_{z2}$.

Nonsymmetric distortions of the molecular frame can break the (local) symmetry selection rules and mix some σ or n character into π orbitals, and vice versa. Vibronic interactions can therefore markedly enhance the probability of El-Sayed-forbidden ISC. In view of the El-Sayed rule, the radiationless $S_1(n\pi^*) \rightsquigarrow T_1(n\pi^*)$ transition of benzophenone, for instance, is not efficient. At first sight, it is surprising that the formation of triplet benzophenone in nonpolar solvents proceeds at a much higher rate than the El-Sayed-allowed $S_1(n\pi^*) \rightsquigarrow T_1(\pi\pi^*)$ transition of fluorenone (70). Two explanations of the fast and efficient triplet population of benzophenone are at hand: (*a*) ISC proceeds in one step from a vibronically coupled $S_1(n\pi^*/\pi\pi^*)$ state to a vibronically coupled $T_1(n\pi^*/\pi\pi^*)$ state, and (*b*) ISC follows a sequential route involving the $T_2(\pi\pi^*)$ state as an intermediate. Femtosecond time-resolved experiments in the gas phase yield a time constant of 5 ps for the $S_1 \rightsquigarrow T_1$ transition, but cannot differentiate between the two models (71). Nonadiabatic surface hopping simulations are not conclusive, either: While Marazzi et al. (56) favor the indirect $S_1 \rightsquigarrow T_2 \rightsquigarrow T_1$ mechanism, Favero et al. (57) consider the direct $S_1 \rightsquigarrow T_1$ route the most important.

3.2. Vibrational Contributions: The Energy Gap Laws

The energy gap laws relate the probability of a unimolecular radiationless transition between an initial and a final electronic state to their adiabatic energy separation and the relative displacements of their potential energy surfaces (see the sidebar titled Energy Gap Laws: Limiting Cases). To simplify the analytic expressions, Englman & Jortner (72) applied a harmonic oscillator model and assumed that the normal modes and their frequencies are the same in the two electronic states, except for displacements in the origins of the normal coordinates.

ENERGY GAP LAWS: LIMITING CASES

For a pair of electronic states whose potential energy surfaces are described by displaced harmonic oscillators, the probability of a unimolecular radiationless transition (*a*) decreases exponentially with increasing energy gap in the weak coupling limit, where the geometric displacement of the two potentials is small, and (*b*) has a Gaussian-shaped dependency on the energy gap at standard temperatures in the strong coupling case, where marked displacements exist in some normal coordinates. In the inverted region, the probability increases with increasing energy gap, runs through a maximum, and decreases again in the normal region.

3.2.1. The weak coupling limit. The geometric dependency of the transition probability is often disregarded in the literature. What is commonly known as the energy gap law is an expression for the probability of a radiationless transition in the weak coupling limit where the relative geometric displacement of the potential energy surfaces is small (**Figure 4*a***). In this limiting case, the FCWD decreases exponentially with increasing adiabatic energy separation ΔE of the two potential energy surfaces according to (72)

$$\text{FCWD} = \frac{1}{\sqrt{2\pi\hbar\omega_M \Delta E}} \exp\left[\frac{-\gamma \Delta E}{\hbar\omega_M}\right]. \qquad 13.$$

Here, ω_M is the maximal vibrational frequency with nonvanishing displacement ΔQ_M, and γ is a positive parameter that contains the pertinent structural information.

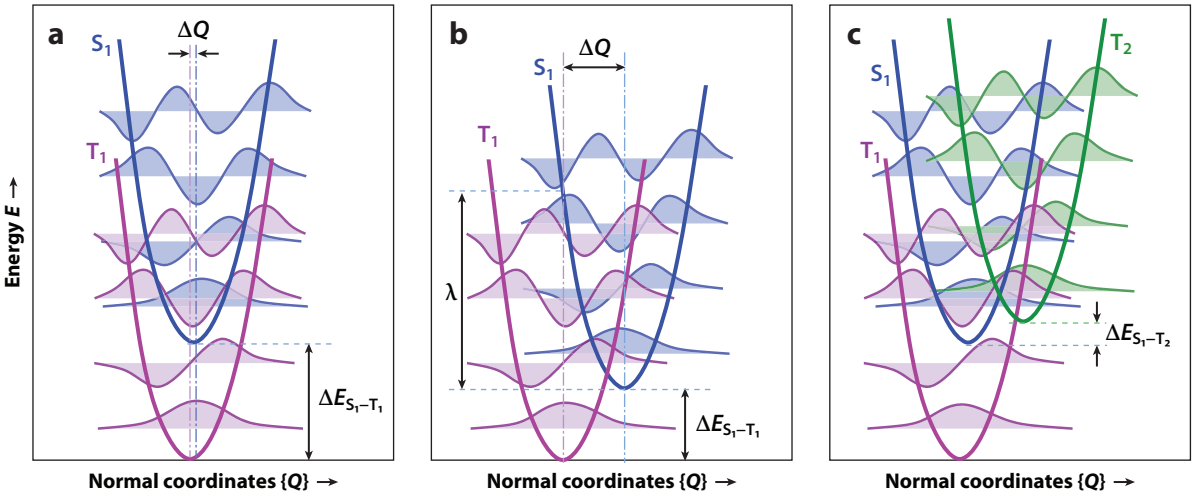

Figure 4

Coupling cases of radiationless $S_1 \rightsquigarrow T_1$ transitions. (*a*) The weak coupling limit. The S_1 and T_1 potentials exhibit small relative displacements in all normal coordinates {*Q*}. Significant overlaps between their vibrational wave functions are obtained only for small singlet–triplet energy separations, $\Delta E_{S_1-T_1}$. The ISC probability decreases exponentially with increasing energy gap. (*b*) The strong coupling case. The S_1 and T_1 potentials exhibit large relative displacements in some coordinates. The ISC probability typically exhibits a Gaussian dependence on $\Delta E_{S_1-T_1} - \lambda$, where λ is the reorganization energy in the S_1 state. In the inverted region, the probability increases with increasing $\Delta E_{S_1-T_1}$ until a maximum is reached at $\Delta E_{S_1-T_1} = \lambda$, where the S_1 and T_1 potentials cross at the S_1 minimum. At even-higher-energy separations, the probability decreases in a regular fashion with increasing $\Delta E_{S_1-T_1}$. (*c*) Second-order spin–vibronic mechanism. Analytical formulas are not available for this case because it employs more than two electronic states. This case is typical of an ISC between nested S_1 and T_1 states mediated by a T_2 state that is energetically near degenerate with S_1 but geometrically displaced in some coordinates. Abbreviation: ISC, intersystem crossing.

For energetically shifted harmonic oscillator potentials with exactly equal vibrational frequencies and vanishing relative displacement of the normal coordinates, the exponential decrease in the transition probability with increasing ΔE is intuitively clear because it is easily shown that the overlap of the corresponding Hermite functions $\langle H_n(Q)|H'_m(Q)\rangle$ vanishes unless $n = m'$. Even in the case of slightly displaced potentials, it is favorable to employ as few vibrational quanta as possible for stepping up the ladder to fulfill the resonance condition in Equation 7. This is why Englman & Jortner (72) focused on the normal modes with maximal frequency in deriving Equation 13. The fewest-steps rule also qualitatively explains the internal deuterium isotope effect on the triplet lifetimes of hydrocarbons. The acceptor modes with the highest frequencies, which act as energy sinks, are C–H stretching modes in these compounds (73). Upon perdeuteration of the emitter, the maximal vibrational frequencies are reduced by a factor of $\sqrt{2}$, thereby reducing the probability of radiationless $T_1 \rightsquigarrow S_0$ decay. Perdeuteration of the solvent environment has a similar impact on phosphorescence lifetimes but is attributed a kinetic origin.

The weak coupling limit is applicable to radiationless transitions between nested states whose potential energy surfaces do not intersect. Such situations are frequently encountered for singlet–triplet pair states with similar electronic structures, for example, ^{1}CT $\rightsquigarrow$ ^{3}CT transitions in TADF OLEDs. As there is no first-order SOC between singlet and triplet states of the same configuration, the electronic coupling term is typically very small, and substantial probability of ISC is expected only in the limit of diminishing $\Delta E_{S_1-T_1}$. Note, however, that spin–vibronic interactions can be substantial and may not be neglected in describing the photophysics of donor–acceptor compounds (18).

3.2.2. The strong coupling case. For pairs of states with unequal electronic structures, pronounced relative displacements are to be expected in some normal coordinates. In this case, termed the strong coupling case by Englman & Jortner (72), overlaps of Hermite functions with different numbers of vibrational quanta do not automatically integrate to zero. Close to the intersection of the potential energy surfaces, the vibrational overlaps become particularly large (**Figure 4*b***), which is why the transition probability does not monotonically decrease with increasing energy gap but rather shows a Gaussian-shaped course. Under standard conditions, the mean vibrational frequency, $\langle\omega\rangle = N^{-1}\sum_j^N \omega_j$, is large in comparison to the temperature T, yielding

$$\mathrm{FCWD} = \frac{1}{\sqrt{2\pi\lambda\hbar\langle\omega\rangle}}\exp\left[\frac{-(\Delta E-\lambda)^2}{2\lambda\hbar\langle\omega\rangle}\right] \qquad 14.$$

in the low-temperature regime. Here, λ is the reorganization energy (compare with **Figure 4*b***). Only in the limit of very high temperatures is normal exponential behavior observed:

$$\mathrm{FCWD} = \frac{1}{\sqrt{4\pi\lambda k_B T}}\exp\left[\frac{-(\Delta E-\lambda)^2}{4\lambda k_B T}\right]. \qquad 15.$$

While these rules give good guidance in general, one must be aware that the harmonic model is completely unrealistic for large energy gaps such as $T_1 \rightsquigarrow S_0$ transitions. Also, the use of the displaced harmonic oscillator model is questionable if the initial and final electronic states have different electronic structures. In a more quantitative ansatz, vibrational frequency shifts and rotations among the normal modes can be taken care of by means of a Duschinsky (74) transformation or similar approaches (75).

4. MODULATION OF INTERSYSTEM CROSSING

Knowing the key factors that control the probability of intersystem crossing does not necessarily mean that their custom-made modulation is an easy task. Trying to increase the ISC rate constant

HEAVY-ATOM EFFECT

According to IUPAC (69), the term heavy-atom effect designates the enhancement of the rate of a spin-forbidden process by the presence of an atom of high atomic number, which is either part of or external to the excited molecular entity.

by chemical substitution effects, such as the replacement of an element by a heavier homolog, for example, can have many side effects on the electronic structure and the energetics of the excited states. Also, temperature effects are often not so clear cut, as they not only accelerate or slow down transitions but also may affect the viscosity of the environment and thereby its ability to adapt to the altered charge distribution of the solute in the excited state. Direct and indirect effects are difficult to distinguish, as they come to pass simultaneously. The following subsections briefly describe the influence of chemical substitution and the molecular environment before discussing their cooperation in greater detail for two sample applications.

4.1. The Heavy-Atom Effect

Owing to the linear dependence of the one-electron SOC Hamiltonian (Equation 2) on the effective nuclear charge Z_ν^{eff} and its inverse cubic dependence on the orbital radius ($r_{j\nu}^{-3}$), spin–orbit coupling constants of atoms strongly increase when moving from left to right or from top to bottom in the periodic table (see the sidebar titled Heavy-Atom Effect). The screening of the interaction by the other electrons causes the scaling to be less steep than Z_ν^4, as may be expected for H-like atoms and ions, but it is markedly higher than linear (37, 38). This does not necessarily mean, however, that the SOCMEs of their molecular compounds follow the same trend.

I restrict the following discussion to electronic effects. Kinetic effects, arising, for example, upon deuteration of a compound, often exert strong influence on the probability of nonradiative deactivation but usually are not subsumed under the term heavy-atom effect.

4.1.1. Internal heavy-atom effect. The enhancement of intercombination transitions of a compound owing to the replacement of a constituent element by a heavier homolog is called the internal heavy-atom effect. In metal–organic complexes of the trivalent ions Al, Sc, Y, La, Gd, and Lu, for example, phosphorescence quantum yields and triplet lifetimes vary markedly, while the energetic positions of the fluorescence and phosphorescence levels are nearly unaffected by the chemical substitution (76). Also, halogenation is known to largely enhance radiative and nonradiative singlet–triplet transitions. In halogenated aromatic hydrocarbons, the phosphorescence-to-fluorescence ratios of $\pi\pi^*$ transitions increase approximately in proportion to the increase in the square of the SOC constant of the substituent atom (77–79).

The internal heavy-atom effect is not always so clear cut, however. In addition to the magnitude of the SOC constant, indirect effects such as energy shifts or changes in the composition of the wave functions play important roles and may lead to counterintuitive trends. For example, in a series of coinage metal complexes, the rate constants of the $S_1 \rightsquigarrow T_1$ ISC and the $T_1 \rightarrow S_0$ radiative decay of the Ag(I) and Au(I) compounds are—despite the larger atomic numbers of the metal cores—smaller than those of the Cu(I) complexes (52, 80, 81). The origin of this behavior is the increased metal-to-ligand CT contribution to the low-lying states of the Cu(I) complexes in comparison to their heavier homologs.

4.1.2. External heavy-atom effect. An enhancement of singlet–triplet transitions may be observed even for unsubstituted aromatic hydrocarbons if they are embedded in alkyl halide matrices or solutions (82). This effect has been termed the external heavy-atom effect to distinguish it from the internal heavy-atom effect observed when the heavy atom is chemically affixed to the molecular skeleton whose intercombinational transitions it perturbs. The effectiveness of the perturbation increases in the order Cl < Br ≪ I (79). Despite many efforts to clarify its origin, the spectroscopic community has not agreed on the underlying reason for the enhanced probability of spin-forbidden transitions. There are two main types of interpretations of the external heavy-atom effect: (*a*) an exchange interaction model between perturber and luminophore, in which S ⇝ T transition intensity is borrowed from electronic transitions of the perturbing halide (83, 84), and (*b*) CT-type mechanisms featuring increased ISC due to donor–acceptor interactions where the luminophore takes the part of either the donor (79, 85) or the acceptor (86, 87). Exciplex formation has also been discussed (88).

4.2. Environment Effects

Solvatochromic response of the solute not only tunes the wavelengths of absorption and emission spectra but also may have a large impact on the rates and even the mechanisms of nonradiative transitions. Solvent–solute interactions have the power to transform a fluorescent dye into an initiator of a photochemical reaction or a triplet sensitizer, and vice versa.

4.2.1. Solvent polarity and reorganization. Whether positive or negative solvatochromism due to a polar medium is observed depends strongly on, among other factors, the magnitude and the orientation of the solute's static dipole moments in the ground and excited states. Therefore, it is not surprising that environment effects are particularly pronounced for CT states. Their emission spectra are known to be very susceptible to the polarity and viscosity of the surrounding medium. In the remainder of Section 4.2, it is assumed that geometry relaxation of the solute in the excited state proceeds at the subpicosecond timescale. Two emission scenarios seem plausible. First, at short time delays after excitation or in rigid environments, the solvent shell is still adapted to the charge distribution of the solute in the electronic ground state. The second scenario applies to longer time delays and less rigid environments. In this case, the solvent molecules can adjust to the charge distribution in the excited state of the solute. In quantum chemical calculations, the first scenario can be simulated by the polarizable continuum model (PCM) (89, 90) or the conductor-like screening model (COSMO) (91), while for the second scenario, corrected linear response (92) or state-specific models (93, 94) have to be employed. In femtosecond time-resolved measurements, solvent reorganization effects become noticeable as time-dependent spectral shifts of the emission. Even in steady-state spectroscopy, the behavior of a donor–acceptor compound may fundamentally differ between liquid and frozen polar solvent environments.

The absorption and early emission spectra of donor–acceptor compounds with almost evenly distributed charge density in the electronic ground state encounter minor solvent shifts with respect to vacuum conditions. A CT transition generates an electronically excited state with large electric dipole moment that favorably interacts with a polar surrounding. Solvent reorganization therefore causes a bathochromic shift of the emission (positive solvatochromicity). More interesting is the behavior of solutes with highly polar charge distribution in the electronic ground state. In the example shown in **Figure 5*a***, the dipole moment of the solute is even reversed upon excitation. Solutes of this type show negative solvatochromicity (hypsochromic shifts) in absorption and in emission at short time delays after excitation because of the unfavorable interaction of the solvent cage with the electric dipole of the solute in the excited state. Solvent reorganization

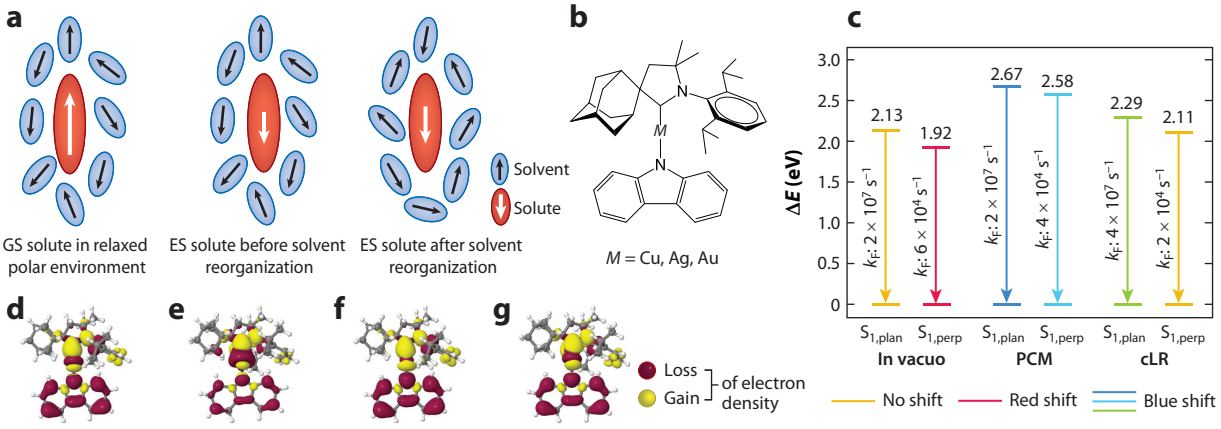

Figure 5

Polarity and solvent reorganization effects on charge-transfer transitions of highly polar carbene metal amides. (*a*) Interaction between the dipole moments of the solute (*white arrows*) and the solvent (*black arrows*) in absorption (*left*), in emission at short time delays after photoexcitation (*middle*), and after solvent reorganization (*right*). (*b*) Chemical structure of the linear CAAC-*M*-Cz complexes. (*c*) Solvent effects on the emission properties of CAAC-Cu-Cz in a chlorobenzene solution employing a polarizable rigid (PCM) or relaxed (cLR) solvent model (81). (*d–g*) Difference densities (isosurface ±0.002) associated with the S_1 and T_1 excitations of CAAC-Cu-Cz. (*d*) S_1^{PCM}. (*e*) T_1^{PCM}. (*f*) S_1^{cLR}. (*g*) T_1^{cLR}. Abbreviations: CAAC, cyclic (alkyl)(amino)-carbene; cLR, corrected linear response; ES, excited state; GS, ground state; PCM, polarizable continuum model. Panel *a* adapted with permission from Reference 16, copyright 2020 American Chemical Society. Panel *c* adapted with permission from Jelena Föller (81).

stabilizes the charge distribution in the excited state while simultaneously destabilizing the electronic ground state. The combined effect causes a red shift of the long-time emission wavelength with respect to the short-time results. Whether the total solvatochromic shift of the steady-state emission with regard to the vacuum results is positive or negative depends on the details.

Figure 5*b* depicts examples of compounds with negative solvatochromicity. The electron-rich carbazolide ligand forms highly polar cyclic (alkyl)(amino)-carbene (CAAC) coinage metal amide complexes. The neutral CAAC-Au-Cz and CAAC-Cu-Cz complexes are excellent TADF-OLED emitters in the solid state (15, 95). The rotationally assisted spin-state inversion (RASI) mechanism, suggested by Di et al. (95) to be responsible for the fast ISC and rISC of the complexes, has attracted particular interest of the scientific community and invoked a series of follow-up investigations from both experimentalists and theoreticians (15, 52, 81, 96–99). Owing to the strong immanent electric dipole moments of the complexes, the crystalline state must be considered a rigid polar environment. Upon excitation to the S_1 or T_1 state, electronic density is transferred from the carbazolide to the CAAC ligand (**Figure 5*d*,*e***). The interligand CT drastically reduces the magnitude of the electric dipole moment and reverses its direction, resulting in pronounced blue shifts of the absorption and early emission with increasing solvent polarity (**Figure 5*c***) (15, 81). In liquid solutions, where the solvent environment can readily adapt to the sudden changes of the solute's charge distribution, a time-dependent red shift of the S_1 emission is observed (15, 95). Although the RASI mechanism turned out to be an artifact of an unbalanced quantum chemical description of the S_1 and T_1 states (96), partially frustrated internal rotation of the carbazolide ligand in the S_1 potential plays a decisive role in the efficient ISC and rISC in these complexes (52, 97, 98).

4.2.2. Hydrogen bonding. In addition to low-lying singlet and triplet ($\pi\pi^*$) states, ($n\pi^*$) states play a decisive role in the photophysics and photochemistry of heteroaromatic organic molecules.

The nonbonding orbitals n typically reside on unsaturated O or N atoms and are fairly localized, whereas the π system extends over larger parts of the molecule. The heteroatom carries a partial negative charge in the ground state. Upon ($n\pi^*$) excitation, the dipole moment is reduced and interacts less favorably with a polar surrounding than the ground-state charge distribution. Electrostatic interactions with polar media therefore result in hypsochromic shifts of the ($n\pi^*$) vertical excitation energy. The marked blue shifts of the ($n\pi^*$) states are even enhanced if the solvent can form H bonds with the unsaturated O and N centers. In mixed heteroaromatic compounds, solvent shifts of ($n_N\pi^*$) transitions are typically somewhat smaller than those of ($n_O\pi^*$) transitions (100).

Flavin, the chromophore of the blue light–sensing proteins, does not only experience solvent shifts of the absorption and emission bands. In a polar protic environment, molecules in the $S_1(\pi\pi^*)$ state no longer have access to the $T_2(n\pi^*)$ state that mediates the fast ISC passage to the $T_1(\pi\pi^*)$ state in nonpolar environments. Instead, the higher-lying $T_3(\pi\pi^*)$ state is stabilized by electrostatic interactions and the ISC mechanism switches from an El-Sayed-allowed direct transition to an El-Sayed-forbidden spin–vibronic one (100).

Similar environment effects have been observed in many aromatic ketones (**Figure 6*a***), which can be regarded as chemical variations of benzophenone. In the more rigid variants, the H atoms in the 2 and 2′ positions of the phenyl groups are replaced by a covalent linkage, either by a direct bond (fluorenone) or by a bridge formed by –CH_2– (anthracenone), –O– (xanthone), –NH– (acridone), or –S– (thioxanthone). While steric repulsion hinders benzophenone from adopting a planar configuration, all other compounds in this family have planar electronic ground states. Their photochemistry and photophysics are shaped by close-lying singlet and triplet ($n\pi^*$) and ($\pi\pi^*$) excited states and their interactions with the solvent or matrix environment. The fluorescence quantum yield of thioxanthone, for example, varies by three orders of magnitude as a function of the solvent (109). Polar solvents cause bathochromic shifts of the lowest ($\pi\pi^*$) states of the aromatic ketones, whereas the ($n\pi^*$) states are shifted hypsochromically. In many cases, aromatic carbonyl compounds fluoresce in polar solvents and do not fluoresce in nonpolar solvents. This observation indicates that the $^1(\pi\pi^*)$ state is the lowest excited singlet state in polar solvents, while in nonpolar solvents the $^1(n\pi^*)$ state, which has little or no oscillator strength, is lowest in energy (110). Whether an aromatic ketone is a good triplet sensitizer depends on the energetic position and the nature of its triplet states. Owing to the stronger exchange interaction of the open shells in ($\pi\pi^*$) states versus ($n\pi^*$) states, the T_1 states of most compounds are $^3(\pi\pi^*)$ states, except for benzophenone and anthracenone, which possess $T_1(n\pi^*)$ states in the crystalline state (111) and in nonpolar solvent environments (70).

Protic solvents form strong H bonds with the carbonyl O. Interactions of the ether (xanthone) or thioether bridges (thioxanthone) with proton donors are much weaker (102, 104). H-bond formation with water molecules at the N–H group of acridone (**Figure 6*b***) appears to have almost no impact on ISC probability, whereas the changes in the S_1–T_2 energy gap are very pronounced in the carbonyl-bonded conformers. Microsolvation experiments in supersonic jets show that two water molecules are sufficient for a level inversion and a substantial slowdown of the ISC (112).

Despite the fact that the aromatic ketones are composed of light elements only, some group members exhibit ultrafast ISC (picosecond timescale) with quantum yields close to one (71, 110, 113, 114), while others are strongly fluorescent (70, 112, 115). Internal heavy-atom effects on the ISC probability are not discernible, because first-order SOC originates predominantly from $n \rightsquigarrow \pi$ interactions of the carbonyl oxygen. It is the intricate competition between different excited-state decay channels (**Figure 6*c–g***), and the possibility of its modulation by a solvent environment and the temperature, that has made the aromatic ketones and their photophysics interesting objects of spectroscopical and quantum chemical investigations.

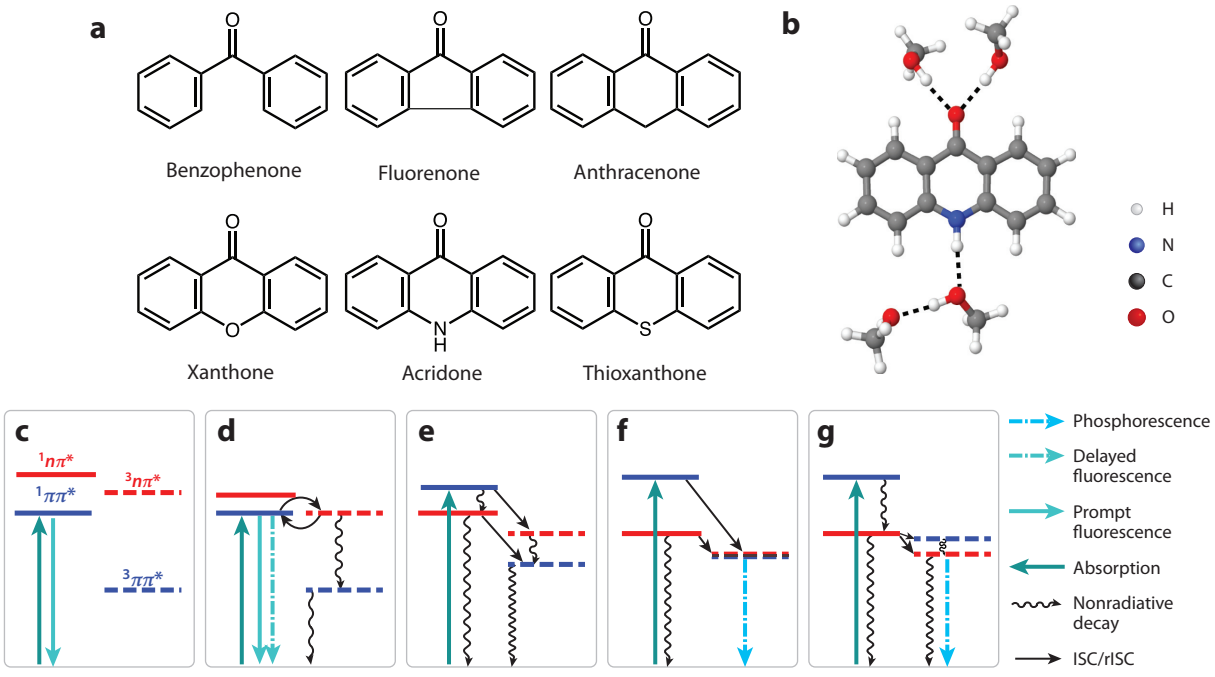

Figure 6

Energy level schemes typical of aromatic ketones, illustrating the competition between radiative and nonradiative excited-state decay pathways. The energetic order of the excited states depends on the chemical composition of the ketone and the environment. (*a*) Aromatic ketones susceptible to the polarity and the H-bonding ability of the solvent. (*b*) Acridone with four H-bonded methanol solvent molecules. (*c*) In polar protic solvents, the $n\pi^*$ states are energetically not accessible from the primarily excited $^1\pi\pi^*$ state. This level scheme applies, for instance, to thioxanthone in trifluoroethanol (101, 102). The major decay channel following photoexcitation is prompt fluorescence. (*d*) The $^3n\pi^*$ and $^1\pi\pi^*$ states have been tuned into resonance, thus promoting fast ISC and rISC between S_1 and T_2, which outcompete $T_2 \rightsquigarrow T_1$ IC. Both prompt and delayed fluorescence have been observed for xanthone in water (103, 104) and for thioxanthone in methanol solution (101, 102, 105). (*e*) Fast ISC quenches the prompt fluorescence and generates long-lived triplet molecules with high yield. Phosphorescence is observed at cryogenic temperatures only. The level scheme is characteristic of a triplet sensitizer, such as thioxanthone (106) or fluorenone (107) in nonpolar environments. (*f*) The $^3n\pi^*$ and $^3\pi\pi^*$ states of xanthone are near-degenerate in nonpolar environments (104, 108). The time constants of the phosphorescence emission are strongly temperature dependent. (*g*) Level scheme corresponding to benzophenone and anthracenone in cyclohexane (70). ISC in benzophenone is ultrafast and populates the T_1 state of mixed $^3\pi\pi^*$ and $^3n\pi^*$ character with a quantum yield close to 1 (71). Abbreviations: IC, internal conversion; ISC, intersystem crossing; rISC, reverse intersystem crossing.

5. CONCLUDING REMARKS

This review aims to provide qualitative insights into the mechanisms and efficiencies of ISC. While SOC-based ISC is clearly the focus, SSC and HFI are described in some detail as well. Not all aspects of ISC could be addressed in this article, nor are all the facets of ISC that have been alluded to understood in full detail. In particular, spin–vibronic and solvent relaxation effects in optoelectronics applications need further attention.

Sample applications are presented and discussed, with particular reference to qualitative rules and their limitations. In many cases, the initial and final electronic states are not the only electronic states involved in the intercombination transition. Intermediate states can participate actively in the ISC if they are energetically accessible, or virtually via second-order SOC or spin–vibronic interactions if they are not. Qualitative rules for estimating the probability of an ISC transition

on the basis of only the character of the initial and final states should therefore be handled with great care.

It is often difficult to determine the energetic positions of optically "dark" states by experiment alone, in particular if they are not the lowest excited states of a given spin multiplicity. Quantum chemistry has been very helpful in this respect. In addition to providing an overview of the energetic ordering of the excited states and their electronic structures, spectroscopic properties such as transition probabilities are invaluable for assigning measured spectral signatures and unraveling the complex kinetic schemes of excited-state processes. Computed rate constants of radiative and nonradiative transitions in principle allow one to discriminate between alternative relaxation mechanisms and pathways, but the outcome of a simulation can be very sensitive with regard to energy shifts. The use of high-level electron correlation methods for calculating the potential energies is therefore mandatory. Ultimately, it is the close collaboration between scientists from different fields that promotes the understanding of relaxation processes in electronically excited species.

DISCLOSURE STATEMENT

The author is not aware of any affiliations, memberships, funding, or financial holdings that might be perceived as affecting the objectivity of this review.

ACKNOWLEDGMENTS

This research was funded by the Deutsche Forschungsgemeinschaft (German Research Foundation) under grant 396890929/GRK 2482.

LITERATURE CITED

1. Tang CW, VanSlyke SA. 1987. Organic electroluminescent diodes. *Appl. Phys. Lett.* 51:913–15
2. Baldo MA, O'Brien DF, You Y, Shoustikov A, Sibley S, et al. 1998. Highly efficient phosphorescent emission from organic electroluminescent devices. *Nature* 395:151–54
3. Kappaun S, Slugovc C, List EJW. 2008. Phosphorescent organic light-emitting devices: working principle and iridium based emitter materials. *Int. J. Mol. Sci.* 9:1527–47
4. Yersin H, Rausch AF, Czerwieniec R, Hofbeck T, Fischer T. 2011. The triplet state of organo-transition metal compounds. Triplet harvesting and singlet harvesting for efficient OLEDs. *Coord. Chem. Rev.* 255:2622–52
5. Choy WCH, Chan WK, Yuan Y. 2014. Recent advances in transition metal complexes and light-management engineering in organic optoelectronic devices. *Adv. Mater.* 26:5368–99
6. Hack M. 2015. Current status of phosphorescent organic light-emitting devices. *SPIE News*, June 30. **https://spie.org/news/5856-current-status-of-phosphorescent-organic-light-emitting-devices?SSO=1**
7. Lee JH, Chen CH, Lee PH, Lin HY, Leung MK, et al. 2019. Blue organic light-emitting diodes: current status, challenges, and future outlook. *J. Mater. Chem. C* 7:5874–88
8. Strassner T. 2016. Phosphorescent platinum(II) complexes with C∧C* cyclometalated NHC ligands. *Acc. Chem. Res.* 49:2680–89
9. Pinter P, Soellner J, Strassner T. 2019. Sky-blue triplet emitters with cyclometalated imidazopyrazine-based NHC ligands and aromatic bulky acetylacetonates. *Chem. Eur. J.* 25:14495–99
10. Lee J, Chen HF, Batagoda T, Coburn C, Djurovich PI, et al. 2016. Deep blue phosphorescent organic light-emitting diodes with very high brightness and efficiency. *Nat. Mater.* 15:92–98
11. Uoyama H, Goushi K, Shizu K, Nomura H, Adachi C. 2012. Highly efficient organic light-emitting diodes from delayed fluorescence. *Nature* 492:234–38

12. Dias FB, Bourdakos KN, Jankus V, Moss KC, Kamtekar KT, et al. 2013. Triplet harvesting with 100% efficiency by way of thermally activated delayed fluorescence in charge transfer OLED emitters. *Adv. Mater.* 25:3707–14
13. Yang Z, Mao Z, Xie Z, Zhang Y, Liu S, et al. 2017. Recent advances in organic thermally activated delayed fluorescence materials. *Chem. Soc. Rev.* 46:915–1016
14. Shi S, Jung MC, Coburn C, Tadle A, Sylvinson MRD, et al. 2019. Highly efficient photo- and electroluminescence from two-coordinate Cu(I) complexes featuring nonconventional N-heterocyclic carbenes. *J. Am. Chem. Soc.* 141:3576–88
15. Hamze R, Peltier JL, Sylvinson MRD, Jung M, Cardenas J, et al. 2019. Eliminating nonradiative decay in Cu(I) emitters: >99% quantum efficiency and microsecond lifetime. *Science* 363:601–6
16. Gernert M, Balles-Wolf L, Kerner F, Müller U, Schmiedel A, et al. 2020. Cyclic (amino)(aryl)carbenes enter the field of chromophore ligands: Expanded π system leads to unusually deep red emitting Cu^{I} compounds. *J. Am. Chem. Soc.* 142:8897–909
17. Dias FB, Santos J, Graves DR, Data P, Nobuyasu RS, et al. 2016. The role of local triplet excited states and D-A relative orientation in thermally activated delayed fluorescence: photophysics and devices. *Adv. Sci.* 3:1600080
18. Penfold TJ, Gindensperger E, Daniel C, Marian CM. 2018. Spin-vibronic mechanism for intersystem crossing. *Chem. Rev.* 118:6975–7025
19. Xu S, Yang Q, Wan Y, Chen R, Wang S, et al. 2019. Predicting intersystem crossing efficiencies of organic molecules for efficient thermally activated delayed fluorescence. *J. Mater. Chem. C* 7:9523–30
20. Nakanotani H, Higuchi T, Furukawa T, Masui K, Morimoto K, et al. 2014. High-efficiency organic light-emitting diodes with fluorescent emitters. *Nat. Commun.* 5:4016–22
21. Furukawa T, Nakanotani H, Inoue M, Adachi C. 2015. Dual enhancement of electroluminescence efficiency and operational stability by rapid upconversion of triplet excitons in OLEDs. *Sci. Rep.* 5:8429
22. Baldo MA, Thompson ME, Forrest SR. 2000. High-efficiency fluorescent organic light-emitting devices using a phosphorescent sensitizer. *Nature* 403:750–53
23. D'Andrade BW, Baldo MA, Adachi C, Brooks J, Thompson ME, Forrest SR. 2001. High-efficiency yellow double-doped organic light-emitting devices based on phosphor-sensitized fluorescence. *Appl. Phys. Lett.* 79:1045–47
24. Heimel P, Mondal A, May F, Kowalsky W, Lennartz C, et al. 2018. Unicolored phosphor-sensitized fluorescence for efficient and stable blue OLEDs. *Nat. Commun.* 9:4990
25. Yao J, Chen Y, Wu Y, Qiao X, Yang D, et al. 2020. High efficiency and low efficiency roll-off all fluorescent white organic light-emitting diodes based on phosphor sensitization. *J. Mater. Chem. C* 8:1666–72
26. Pauli W. 1927. Zur Quantenmechanik des magnetischen Elektrons. *Z. Phys.* 43:601–28
27. Marian CM. 2001. Spin-orbit coupling in molecules. In *Reviews in Computational Chemistry*, Vol. 17, ed. KB Lipkowitz, DB Boyd, pp. 99–204. New York: Wiley
28. Moss R. 1997. *Advanced Molecular Quantum Mechanics*. Dordrecht, Neth.: Springer
29. Sakurai JJ. 1993. *Modern Quantum Mechanics*. New York: Addison-Wesley
30. Dyall KG, Fægri K Jr. 2007. *Introduction to Relativistic Quantum Chemistry*. Oxford, UK: Oxford Univ. Press
31. Reiher M, Wolf A, eds. 2009. *Relativistic Quantum Chemistry: The Fundamental Theory of Molecular Science*. New York: Wiley
32. Hess BA, Marian CM, Wahlgren U, Gropen O. 1996. A mean-field spin-orbit method applicable to correlated wavefunctions. *Chem. Phys. Lett.* 251:365–71
33. Berning A, Werner HJ, Schweizer M, Knowles PJ, Palmieri P. 2000. Spin-orbit matrix elements for internally contracted multireference configuration interaction wavefunctions. *Mol. Phys.* 98:1823–33
34. Neese F. 2005. Efficient and accurate approximations to the molecular spin-orbit coupling operator and their use in molecular g-tensor calculations. *J. Chem. Phys.* 122:034107
35. Samzow R, Hess BA. 1991. Spin-orbit effects in the Br atom in the framework of the no-pair theory. *Chem. Phys. Lett.* 184:491–96
36. van Lenthe E, Snijders JG, Baerends EJ. 1996. The zero-order regular approximation for relativistic effects: the effect of spin-orbit coupling in closed shell molecules. *J. Chem. Phys.* 105:6505–16

37. Koseki S, Gordon MS, Schmidt MW, Matsunaga N. 1995. Main group effective nuclear charges for spin-orbit calculations. *J. Phys. Chem.* 99:12764–72
38. Koseki S, Schmidt MW, Gordon MS. 1998. Effective nuclear charges for the first- through third-row transition metal elements in spin–orbit calculations. *J. Phys. Chem. A* 102:10430–35
39. Christiansen PA, Ermler WC, Pitzer KS. 1985. Relativistic effects in chemical systems. *Annu. Rev. Phys. Chem.* 36:407–32
40. Cundari TR, Benson MT, Lutz ML, Sommerer SO. 1996. Effective core potential approaches to the chemistry of the heavier elements. In *Reviews in Computational Chemistry*, Vol. 8, ed. KB Lipkowitz, DB Boyd, pp. 145–202. New York: Wiley
41. Dolg M. 2000. Effective core potentials. In *Modern Methods and Algorithms of Quantum Chemistry*, ed. J Grotendorst, pp. 479–508. NIC Ser. Vol. 1. Jülich, Ger.: John von Neumann Inst. Comput.
42. Pitzer RM, Winter NW. 1988. Electronic-structure methods for heavy-atom molecules. *J. Phys. Chem.* 92:3061–63
43. Kleinschmidt M, van Wüllen C, Marian CM. 2015. Intersystem-crossing and phosphorescence rates in fac-Ir^{III} $(ppy)_3$: a theoretical study involving multi-reference configuration interaction wavefunctions. *J. Chem. Phys.* 142:094301
44. Cheng YY, Fückel B, Khoury T, Clady RGCR, Tayebjee MJY, et al. 2010. Kinetic analysis of photochemical upconversion by triplet-triplet annihilation: beyond any spin statistical limit. *J. Phys. Chem. Lett.* 1:1795–99
45. Schmidt TW, Castellano FN. 2014. Photochemical upconversion: the primacy of kinetics. *J. Phys. Chem. Lett.* 5:4062–72
46. Tayebjee MJY, Sanders SN, Kumarasamy E, Campos LM, Sfeir MY, McCamey DR. 2017. Quintet multiexciton dynamics in singlet fission. *Nat. Phys.* 13:182–88
47. Sakai H, Inaya R, Nagashima H, Nakamura S, Kobori Y, et al. 2018. Multiexciton dynamics depending on intramolecular orientations in pentacene dimers: recombination and dissociation of correlated triplet pairs. *J. Phys. Chem. Lett.* 9:3354–60
48. Musser AJ, Clark J. 2019. Triplet-pair states in organic semiconductors. *Annu. Rev. Phys. Chem.* 70:323–51
49. Ogiwara T, Wakikawa Y, Ikoma T. 2015. Mechanism of intersystem crossing of thermally activated delayed fluorescence molecules. *J. Phys. Chem. A* 119:3415–18
50. Etherington MK, Gibson J, Higginbotham HF, Penfold TJ, Monkman AP. 2016. Revealing the spin-vibronic coupling mechanism of thermally activated delayed fluorescence. *Nat. Commun.* 7:13680
51. Gibson J, Monkman AP, Penfold TJ. 2016. The importance of vibronic coupling for efficient reverse intersystem crossing in thermally activated delayed fluorescence molecules. *Chem. Phys. Chem.* 17:2956–61
52. Eng J, Penfold TJ. 2020. Understanding and designing thermally activated delayed fluorescence emitters: beyond the energy gap approximation. *Chem. Rec.* 20:1–27
53. Capano G, Chergui M, Rothlisberger U, Tavernelli I, Penfold TJ. 2014. A quantum dynamics study of the ultrafast relaxation in a prototypical Cu(I)–phenanthroline. *J. Phys. Chem. A* 118:9861–69
54. Cui G, Thiel W. 2014. Generalized trajectory surface-hopping method for internal conversion and intersystem crossing. *J. Chem. Phys.* 141:124101
55. Mai S, Marquetand P, González L. 2015. A general method to describe intersystem crossing dynamics in trajectory surface hopping. *Int. J. Quantum Chem.* 115:1215–31
56. Marazzi M, Mai S, Roca-Sanjuán D, Delcey MG, Lindh R, et al. 2016. Benzophenone ultrafast triplet population: revisiting the kinetic model by surface-hopping dynamics. *J. Phys. Chem. Lett.* 7:622–26
57. Favero L, Granucci G, Persico M. 2016. Surface hopping investigation of benzophenone excited state dynamics. *Phys. Chem. Chem. Phys.* 18:10499–506
58. Fumanal M, Plasser F, Mai S, Daniel C, Gindensperger E. 2018. Interstate vibronic coupling constants between electronic excited states for complex molecules. *J. Chem. Phys.* 148:124119
59. van Veenendaal M. 2020. Dissipation and dynamics in ultrafast intersystem crossings. *J. Chem. Phys.* 152:024104
60. Etinski M, Tatchen J, Marian CM. 2014. Thermal and solvent effects on the triplet formation in cinnoline. *Phys. Chem. Chem. Phys.* 16:4740–51

61. Henry BR, Siebrand W. 1971. Spin-orbit coupling in aromatic hydrocarbons. Analysis of nonradiative transitions between singlet and triplet states in benzene and naphthalene. *J. Chem. Phys.* 54:1072–85
62. Peng Q, Niu Y, Shi Q, Gao X, Shuai Z. 2013. Correlation function formalism for triplet excited state decay: combined spin–orbit and nonadiabatic couplings. *J. Chem. Theory Comput.* 9:1132–43
63. Etinski M, Rai-Constapel V, Marian CM. 2014. Time-dependent approach to spin-vibronic coupling: implementation and assessment. *J. Chem. Phys.* 140:114104
64. de Souza B, Farias G, Neese F, Izsák R. 2019. Predicting phosphorescence rates of light organic molecules using time-dependent density functional theory and the path integral approach to dynamics. *J. Chem. Theory Comput.* 15:1896–904
65. Lawetz V, Orlandi G, Siebrand W. 1972. Theory of intersystem crossing in aromatic hydrocarbons. *J. Chem. Phys.* 56:4058–72
66. Marian CM. 2016. Mechanism of the triplet-to-singlet upconversion in the assistant dopant ACRXTN. *J. Phys. Chem. C* 120:3715–21
67. El-Sayed MA. 1962. The radiationless processes involving change of multiplicity in the diazenes. *J. Chem. Phys.* 36:573–74
68. El-Sayed MA. 1963. Spin-orbit coupling and the radiationless processes in nitrogen heterocyclics. *J. Chem. Phys.* 38:2834–38
69. McNaught AD, Wilkinson A. 1997. *Compendium of Chemical Terminology*. New York: Blackwell Sci. 2nd ed.
70. Kobayashi T, Nagakura S. 1976. Picosecond time-resolved spectroscopy and the intersystem crossing rates of anthrone and fluorenone. *Chem. Phys. Lett.* 43:429–34
71. Spighi G, Gaveau MA, Mestdagh JM, Poisson L, Soep B. 2014. Gas phase dynamics of triplet formation in benzophenone. *Phys. Chem. Chem. Phys.* 16:9610–18
72. Englman R, Jortner J. 1970. The energy gap law for radiationless transitions in large molecules. *Mol. Phys.* 18:145–64
73. Lin SH, Bersohn R. 1968. Effect of partial deuteration and temperature on triplet-state lifetimes. *J. Chem. Phys.* 48:2732–36
74. Duschinsky F. 1937. The importance of the electron spectrum in multi atomic molecules concerning the Frank–Condon principle. *Acta Physicochim.* 7:551–66
75. Reimers JR. 2001. A practical method for the use of curvilinear coordinates in calculations of normal-mode-projected displacements and Duschinsky rotation matrices for large molecules. *J. Chem. Phys.* 115:9103–9
76. Yuster P, Weissman SI. 1949. Effects of perturbations on phosphorescence: luminescence of metal organic complexes. *J. Chem. Phys.* 17:1182–88
77. McClure DS. 1949. Triplet–singlet transitions in organic molecules. Lifetime measurements of the triplet state. *J. Chem. Phys.* 17:905–13
78. Kasha M. 1950. Characterization of electronic transitions in complex molecules. *Discuss. Faraday Soc.* 9:14–19
79. McGlynn SP, Sunseri R, Christodouleas N. 1962. External heavy-atom spin–orbital coupling effect. I. The nature of the interaction. *J. Chem. Phys.* 37:1818–24
80. Hsu CW, Lin CC, Chung MW, Chi Y, Lee GH, et al. 2011. Systematic investigation of the metal-structure–photophysics relationship of emissive d^{10}-complexes of group 11 elements: the prospect of application in organic light emitting devices. *J. Am. Chem. Soc.* 133:12085–99
81. Föller J. 2018. *Quantum chemical investigation of coinage metal complexes with regard to their application in OLEDs*. PhD Thesis, Heinrich Heine Univ., Düsseldorf, Ger.
82. Kasha M. 1952. Collisional perturbation of spin-orbital coupling and the mechanism of fluorescence quenching. A visual demonstration of the perturbation. *J. Chem. Phys.* 20:71–74
83. Giachino GG, Kearns DR. 1970. Nature of the external heavy-atom effect on radiative and nonradiative singlet-triplet transitions. *J. Chem. Phys.* 52:2964–74
84. Komada Y, Yamauchi S, Hirota N. 1985. Mechanisms of external heavy atom effects on the lowest excited triplet states: naphthalene and biphenyl X traps. *J. Chem. Phys.* 82:1651–60
85. McGlynn SP, Daigre J, Smith FJ. 1963. External heavy-atom spin–orbital coupling effect. IV. Intersystem crossing. *J. Chem. Phys.* 39:675–79

86. Chandra AK, Turro NJ, Lyons AL, Stone P. 1978. The intramolecular external heavy atom effect in bromo-, benzo-, and naphthonorbornenes. *J. Am. Chem. Soc.* 100:4964–68
87. Minaev BF, Knuts S, Ågren H. 1994. On the interpretation of the external heavy atom effect on singlet–triplet transitions. *Chem. Phys.* 181:15–28
88. Shimizu Y, Azumi T. 1982. Mechanism of external heavy atom effect on intersystem crossing in fluid solutions. Analysis based on fluorescence decay data. *J. Phys. Chem.* 86:22–26
89. Mennucci B, Cancès E, Tomasi J. 1997. Evaluation of solvent effects in isotropic and anisotropic dielectrics and in ionic solutions with a unified integral equation method: theoretical bases, computational implementation, and numerical applications. *J. Phys. Chem. B* 101:10506
90. Tomasi J, Mennucci B, Cammi R. 2005. Quantum mechanical continuum solvation models. *Chem. Rev.* 105:2999–3094
91. Klamt A, Schüürmann G. 1993. COSMO: a new approach to dielectric screening in solvents with explicit expressions for the screening energy and its gradient. *J. Chem. Soc. Perkin Trans.* 2:799–805
92. Caricato M, Mennucci B, Tomasi J, Ingrosso F, Cammi R, et al. 2006. Formation and relaxation of excited states in solution: a new time dependent polarizable continuum model based on time dependent density functional theory. *J. Chem. Phys.* 124:124520
93. Cammi R, Corni S, Mennucci B, Tomasi J. 2005. Electronic excitation energies of molecules in solution: state specific and linear response methods for nonequilibrium continuum solvation models. *J. Chem. Phys.* 122:104513
94. Mewes JM, Herbert JM, Dreuw A. 2017. On the accuracy of the general, state-specific polarizable-continuum model for the description of correlated ground- and excited states in solution. *Phys. Chem. Chem. Phys.* 19:1644–54
95. Di D, Romanov AS, Yang L, Richter JM, Rivett JPH, et al. 2017. High-performance light-emitting diodes based on carbene–metal–amides. *Science* 356:159–63
96. Föller J, Marian CM. 2017. Rotationally assisted spin-state inversion in carbene–metal–amides is an artifact. *J. Phys. Chem. Lett.* 8:5643–47
97. Thompson S, Eng J, Penfold TJ. 2018. The intersystem crossing of a cyclic (alkyl)(amino) carbene gold(I) complex. *J. Chem. Phys.* 149:014304
98. Eng J, Thompson S, Goodwin H, Credgington D, Penfold TJ. 2020. Competition between the heavy atom effect and vibronic coupling in donor–bridge–acceptor organometallics. *Phys. Chem. Chem. Phys.* 22:4659–67
99. Lüdtke N, Föller J, Marian CM. 2020. Understanding the luminescence properties of Cu(I) complexes: a quantum chemical perusal. *Phys. Chem. Chem. Phys.* 22:23530–44
100. Salzmann S, Tatchen J, Marian CM. 2008. The photophysics of flavins: What makes the difference between gas phase and aqueous solution? *J. Photochem. Photobiol. A* 198:221–31
101. Villnow T, Ryseck G, Rai-Constapel V, Marian CM, Gilch P. 2014. Chimeric behavior of excited thioxanthone in protic solvents. I. Experiments. *J. Phys. Chem. A* 118:11696–707
102. Rai-Constapel V, Villnow T, Ryseck G, Gilch P, Marian CM. 2014. Chimeric behavior of excited thioxanthone in protic solvents. II. Theory. *J. Phys. Chem. A* 118:11708–17
103. Heinz B, Schmidt B, Root C, Satzger H, Milota F, et al. 2006. On the unusual fluorescence properties of xanthone in water. *Phys. Chem. Chem. Phys.* 8:3432–39
104. Rai-Constapel V, Etinski M, Marian CM. 2013. Photophysics of xanthone: a quantum chemical perusal. *J. Phys. Chem. A* 117:3935–44
105. Torres Ziegenbein C, Fröbel S, Glöß M, Nobuyasu RS, Data P, et al. 2017. Triplet harvesting with a simple aromatic carbonyl. *Chem. Phys. Chem.* 18:2314–17
106. Mundt R, Villnow T, Ziegenbein CT, Gilch P, Marian C, Rai-Constapel V. 2016. Thioxanthone in apolar solvents: Ultrafast internal conversion precedes fast intersystem crossing. *Phys. Chem. Chem. Phys.* 18:6637–47
107. Soep B, Mestdagh JM, Briant M, Gaveau MA, Poisson L. 2016. Direct observation of slow intersystem crossing in an aromatic ketone, fluorenone. *Phys. Chem. Chem. Phys.* 18:22914–20
108. McMorrow D, Wyche MI, Chou PT, Kasha M. 2015. On the dual phosphorescence of xanthone and chromone in glassy hydrocarbon hosts. *Photochem. Photobiol.* 91:576–85

109. Dalton JC, Montgomery FC. 1974. Solvent effects on thioxanthone fluorescence. *J. Am. Chem. Soc.* 96:6230–32
110. Cavaleri JJ, Prater K, Bowman RM. 1996. An investigation of the solvent dependence on the ultrafast intersystem crossing kinetics of xanthone. *Chem. Phys. Lett.* 259:495–502
111. Udagawa Y, Azumi T, Ito M, Nagakura S. 1968. Phosphorescence and triplet←singlet absorption spectra of benzophenone crystal at 4.2°K. *J. Chem. Phys.* 49:3764–71
112. Mitsui M, Ohshima Y, Kajimoto O. 2000. Structure and dynamics of 9(10H)-acridone and its hydrated clusters. III. Microscopic solvation effects on nonradiative dynamics. *J. Phys. Chem. A* 104:8660–70
113. Hochstrasser RM, Lutz H, Scott GW. 1974. The dynamics of populating the lowest triplet state of benzophenone following singlet excitation. *Chem. Phys. Lett.* 24:162–67
114. Anderson R, Hochstrasser R, Lutz H, Scott G. 1974. Measurements of intersystem crossing kinetics using 3545 Å picosecond pulses: nitronaphthalenes and benzophenone. *Chem. Phys. Lett.* 28:153–57
115. Hagiwara Y, Hasegawa T, Shoji A, Kuwahara M, Ozaki H, Sawai H. 2008. Acridone-tagged DNA as a new probe for DNA detection by fluorescence resonance energy transfer and for mismatch DNA recognition. *Bioorg. Med. Chem.* 16:7013–20